1 **Cost evaluation and sensitivity analysis of the alkaline zinc-iron flow battery**
2 **system for large-scale energy storage applications**
3

4 Ziqi Chen[a], Yongfu Liu[a,b], Wentao Yu[a], Qijiao He[c], Meng Ni[c], Shuquan Yang[d],
5 Shuanglin Zhang[d], Peng Tan[a*]
6

7 [a.] Department of Thermal Science and Energy Engineering, University of Science
8 and Technology of China (USTC), Hefei 230026, Anhui, China.
9 [b.] Shanghai JINGYI Electrical Apparatus Factory Co., Ltd. Shanghai 201700, China.
10 [c.] Department of Building and Real Estate, Research Institute for Sustainable Urban
11 Development (RISUD) & Research Institute for Smart Energy (RISE), The Hong
12 Kong Polytechnic University, Hung Hom, Kowloon, Hong Kong, China.
13 [d.] Anhui Conch New Energy Co., Ltd, Wuhu 241000, Anhui, China.
14 * Corresponding author:
15 Email: pengtan@ustc.edu.cn (Peng Tan)
16

17 **Abstract:** Alkaline zinc-iron flow batteries attract great interest for remarkable energy

18 density, high safety, environmentally benign. However, comprehensive cost evaluation

19 and sensitivity analysis of this technology are still absent. In this work, a cost model for

20 a 0.1 MW/0.8 MWh alkaline zinc-iron flow battery system is presented, and a capital

21 cost under the U.S. Department of Energy's target cost of 150 $ per kWh is achieved.

22 Besides, the effects of electrode geometry, operating conditions, and membrane types

23 on the system cost are investigated. The results illustrate that a low flow rate and thin

24 electrodes with high porosity contribute to low capital costs under low current densities.

25 Furthermore, the porous polybenzimidazole (PBI) membrane is more cost-effective

26 than Nafion 212 membrane. This work provides an integrated estimation for the zinc-

27 iron flow battery system, demonstrating its tremendous potential for grid-level energy

28 storage applications.

29 **Keywords:** Zinc-iron redox flow battery; Large-scale energy storage; System cost;

30 Sensitivity analysis

1. Introduction

To address the pollution, rising energy costs, and climate change caused by the intensive use of fossil fuels, tremendous attention has been paid to alternative, renewable energy such as solar and wind energy [1–3]. For instance, 95% of new energy consumption in Europe from 2005 to 2030 will come from renewable energy sources [4]. However, the intermittent and unreliable characteristic of this kind of energy triggers the pursuit of energy storage technologies with competitive cost and high reliability [4–7].

Flow batteries, of which the energy and power can be designed independently, combine excellent traits of great safety, high efficiency, and durable cycle life, becoming a promising candidate for the back power of renewable energy sources [8–10]. Since Thaller proposed the first iron-chromium (Fe-Cr) flow battery in 1975 [11], various kinds of flow batteries have been invented and advanced, for instance, all vanadium (V-V) flow batteries [12–20], zinc-based flow batteries [21–25], iron-based flow batteries [26–30], and polymer-based flow batteries [31–35]. To balance the variability of electricity load and meet the rapid growth of energy needs, energy storage over GWh magnitude is pursued [36]. The U.S. Department of Energy (DOE) proposed a long-term target for energy storage technologies of a system capital cost under 150 $ kWh^{-1} [37]. For this purpose, numerous works have been performed to give comprehensive cost analyses on flow battery systems for large power capacity and low capital cost. The Pacific Northwest National Laboratory (PNNL) developed a cost-performance model for V-V and iron-vanadium (Fe-V) redox flow batteries and

53   determined the optimal chemistry and operating conditions for desired power or energy,

54   from which the V-V chemistry and the Fe-V chemistry are the optimum options for

55   energy-intensive and power-intensive applications, respectively [36]. Zeng et al.

56   conducted a comparative study for V-V and iron-chromium (Fe-Cr) redox flow batteries

57   on the cost and performance of the 1 MW-8 h system. It was found that the Fe-Cr system

58   shows a more serious capacity decline than the V-V system and is more cost-effective

59   at a higher range of power densities and capacities [38]. Singh et al. investigated the

60   levelized cost of a hydrogen-bromine (H-Br) flow battery system with different

61   configurations and performed sensitivity analyses on the system components. The

62   lowest system capital cost of 220 \$ kWh^{-1} is achieved for a four-hour discharge system,

63   and extending the lifetime of electrocatalysts is needed [39]. Gong et al. presented a 1

64   MW/8 MWh zinc-iron (Zn-Fe) flow battery system utilizing twofold membranes with

65   threefold electrolytes, achieving a system cost lower than \$100 kWh^{-1} [40].

66   From the perspective of research and development, the dominated flow battery at

67   present is still the V-V redox flow battery. Plentiful experimental and numerical studies

68   have been carried out to improve its performance. For instance, Yoon et al. inserted an

69   additional electrode layer at the entrance and exit of a V-V redox flow battery to

70   manipulate the regional porosity, and proposed an empirical equation to optimize the

71   local electrode porosity distribution, through which, the energy efficiency of the cell

72   can be increased to 67.7% at 150 mA cm^{-2} [2]. Sun et al. established a three-

73   dimensional, multi-physical model to explore the flow field design for large-scale V-V

74   redox flow batteries. The results suggested that the cell with a split-interdigitated flow

3

field achieved the highest overall energy efficiency, causing the increase of pressure

drop losses [18]. However, the expensive chemical cost, high demand for the purity of

vanadium, and temperature-constrained inferior solubility of redox species hamper the

commercialization of the V-V redox flow batteries [41]. Zn-Fe flow batteries, feature

the advantages of abundant zinc metal reserve, high energy density, and low price,

becoming a promising alternative to V-V flow batteries. Over the past 20 years,

enormous efforts have been devoted to zinc-iron flow batteries and huge progress has

been made. Yuan et al. proposed an alkaline Zn-Fe flow battery that achieved steady

performance for more than 500 cycles with a self-made porous PBI membrane and a

three-dimensional porous carbon felt electrode. Besides, a kilowatt cell stack with a

capital cost lower than 90 $ kWh^{-1} was constructed [42]. In their other work, a

nanoporous membrane with negative charges is developed for alkaline Zn-Fe flow

batteries, with which the battery can operate stably for 240 cycles at a current density

of 80 to 160 mA cm^{-2} [43]. Chang et al. presented an alkaline Zn-Fe flow battery based

on a cost-effective membrane with highly anti-alkali microporous hollow spheres,

exhibiting 500 stable cycles with coulombic efficiency of 98.6% and energy efficiency

of 88.3% at 80 mA cm^{-2} [44]. Xie et al. proposed a neutral Zn-Fe flow battery utilizing

highly soluble $FeCl_2/ZnBr_2$ species, exhibiting steady performance for over 100

cycles and a charge energy density of 56.3 Wh L^{-1} [45]. However, few studies have

been performed on the cost prediction for this technology. Despite the cost of the

double-membrane triple-electrolyte design is attractive [40], its complex configuration

can be a huge barrier to further industrialization. Therefore, a comprehensive estimate

4

97 　of the capital cost of a Zn-Fe flow battery system with a conventional two-electrolyte

98 　structure is in great demand.

99 　　Herein, we provided a cost model for an alkaline Zn-Fe flow battery system

100 　following our previous work [46]. First, a stationary, two-dimensional electrochemical

101 　model for a Zn-Fe flow battery was established. After model validation, the capital cost

102 　for a 0.1 MW/0.8 MWh Zn-Fe flow battery system was calculated considering the shunt

103 　losses and pumping losses. Moreover, a sensitivity analysis for the battery system is

104 　performed to deeply understand the influences of the operating conditions and cell

105 　components on the system economy. This work presents a powerful approach to

106 　estimate the feasibility of the Zn-Fe flow battery system as well as offering guidance

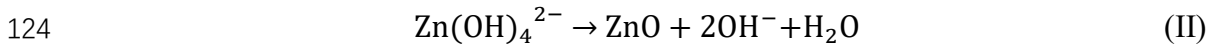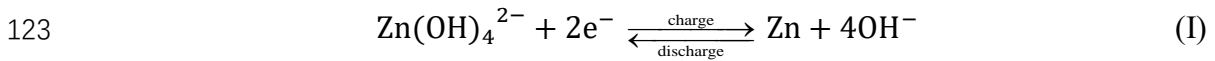107 　for practical applications.

108 **2.　Model development**
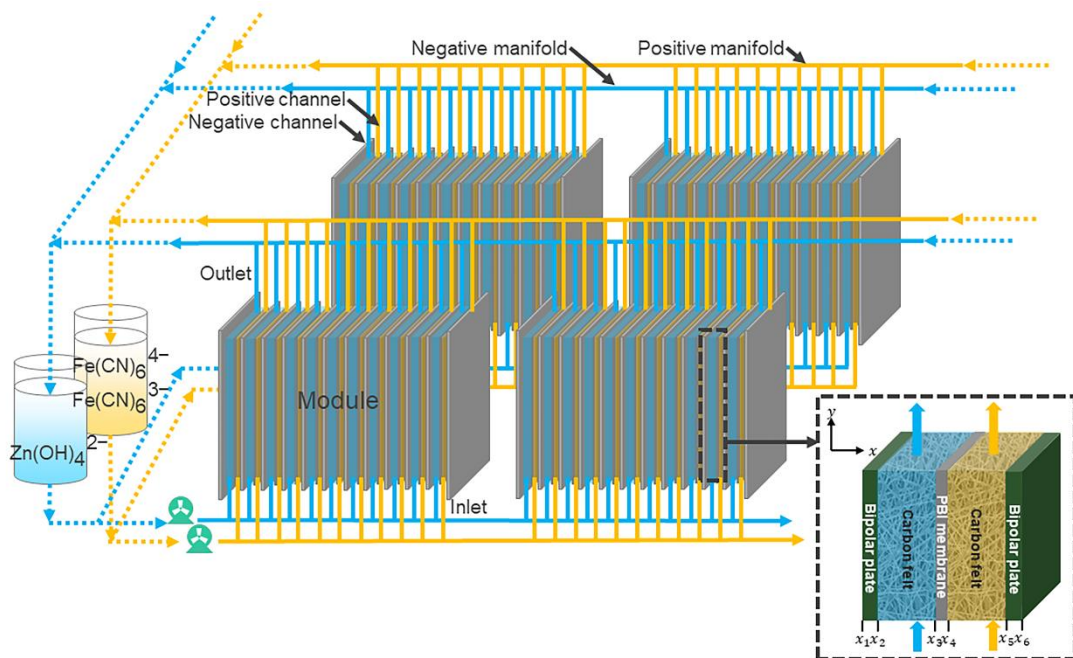
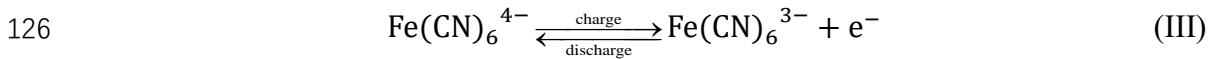**Fig. 1** Schematic of a zinc-iron flow battery stack.

112   Fig. 1 displays the configuration of a Zn-Fe flow battery stack. The system is

113   constructed of modules connected in 5 series and 5 parallels to meet the desired power

114   output of 0.1 MW, in which each module contains 11 single cells connected by bipolar

115   plates. The positive electrolyte consists of $Fe(CN)_6^{3-}/Fe(CN)_6^{4-}$ redox pair and a

116   KOH solution, while the negative electrolyte contains $Zn(OH)_4^{2-}/$ Zn redox pair and

117   a NaOH solution. Porous carbon felts are adopted as the electrodes and sandwich a PBI

118   membrane to separate the negative and positive electrolytes. Gaskets are used between

119   the contiguous components to avoid electrolyte leakage. The electrolytes are contained

120   in separate external reservoirs and circulated through a complex pipe system with the

121   drive of pumps. The electrochemical reactions are as follows:

122   Negative electrode:

123
$$Zn(OH)_4^{2-} + 2e^- \xrightleftharpoons[\text{discharge}]{\text{charge}} Zn + 4OH^- \tag{I}$$

124
$$Zn(OH)_4^{2-} \rightarrow ZnO + 2OH^- + H_2O \tag{II}$$

125   Positive electrode:

126
$$Fe(CN)_6^{4-} \xrightleftharpoons[\text{discharge}]{\text{charge}} Fe(CN)_6^{3-} + e^- \tag{III}$$

127   During charge, $Zn(OH)_4^{2-}$ reduction reaction takes place on the negative

128   electrode, forming the deposition of metallic zinc. In the discharging process, zinc gains

129   two electrons oxidized to $Zn(OH)_4^{2-}$ ions, then $Zn(OH)_4^{2-}$ ions accumulate

130   increasingly and convert to ZnO once saturated. In this work, the predominant reaction

131   at the negative electrode is assumed to be the transformation between $Zn(OH)_4^{2-}$ ions

132   and zinc (Reaction I) with neglecting the existence of solid ZnO because the adopted

133   concentration of $Zn(OH)_4^{2-}$ is lower than its saturation value [47]. In the positive

134   half-cell, the $Fe(CN)_6^{4-}$ oxidation reaction and the $Fe(CN)_6^{3-}$ reduction reaction

135   take place during charge and discharge, respectively (Reaction III).

Several assumptions are made for simplification during simulation:

1. The whole cell is assumed to be isothermal.

2. Incompressible fluid is utilized for electrolyte flow.

3. All physical properties are considered isotropic and homogeneous.

4. Hydrogen evolution reaction (HER) and oxygen evolution reaction (OER) are not considered.

5. Dilute solution hypothesis is adopted for mass transfer.

6. Changes of concentration, potential, and pressure along the width of the cell are ignored.

7. The variation of electrolyte volume driven by water transfer through the membrane is neglected.

This model combines an electrochemical model with a pumping loss model and a shunt current model. For a specific current density, the relationship between the electrochemical voltage and the current density is calculated with an assumed stack area. Then, the pump loss and the shunt loss are calculated to get the effective voltage and associated power. Adjustments for flow rates and flow channel geometry are made to achieve as high a voltage as possible. When the calculated power is less than 0.1 MW, the stack area is increased and this process repeats. Once the required power is reached, the area is fixed to determine the stack component costs. Next, the electrolyte costs are determined based on the electrolyte volume needed for the 0.8 MWh output energy. All calculations above are performed at the 50% SOC for simplification.

2.1 Electrochemical model

158　　　The detailed electrochemical model with the dissolution-deposition process has

159　　been developed in our previous work [46]. Here, only the main governing equations

160　　and boundary conditions are presented.

161　　**2.1.1 Governing equations**

162　　　The ionic and electronic current densities at all domains of the cell obey the charge

163　　conservation:

164
$$\nabla \cdot \vec{j_l^e} + \nabla \cdot \vec{j_s^e} = 0 \tag{1}$$

165　　where $\vec{j_l^e}$ and $\vec{j_s^e}$ are given by the following equations:

166
$$\vec{j_l^e} = F \sum_i z_i \vec{N_i^e} \tag{2}$$

167
$$\vec{j_s^e} = \sigma_s^e \nabla \phi_s^e \tag{3}$$

168　　in which F denotes the Faraday constant, z_i and $\vec{N_i^e}$ denote the valence and flux of

169　　species i, respectively. The Nernst-Planck equation is employed to describe the flux $\vec{N_i^e}$

170　　and consists of diffusion, migration and convection in three terms:

171
$$\vec{N_i^e} = -D_i^{eff}\nabla c_i^e - z_i u_i^e c_i^e F \nabla \phi_l^e + \vec{v_l^e} c_i^e \tag{4}$$

172　　where u_i^e represents the ionic mobility, c_i^e the concentration of species i, ϕ_l^e the

173　　electrolyte potential, and $\vec{v_l^e}$ the velocity vector. The effective diffusion coefficient

174　　D_i^{eff} is corrected from the diffusion coefficient D_i using the Bruggemann relation:

175
$$D_i^{eff} = \varepsilon^{3/2} D_i \tag{5}$$

176　　　where ε is the electrode porosity.

177　　　The Butler-Volmer equations are adopted to describe the reversible

178　　electrochemical reactions at the electrode surfaces:

179
$$FD_{Fe^{2+}}\left(\frac{c_{Fe^{2+}}^e - c_{Fe^{2+}}^s}{r_p}\right) = Fk_+ (c_{Fe^{2+}}^e)^{(1-\alpha_+)}(c_{Fe^{3+}}^e)^{\alpha_+}\left[\left(\frac{c_{Fe^{2+}}^s}{c_{Fe^{2+}}^e}\right)\exp\left(\frac{(1-\alpha_+)F\eta_-}{RT}\right) - \right.$$

$$\left(\frac{c^s_{Fe^{3+}}}{c^e_{Fe^{3+}}}\right)\exp\left(\frac{-\alpha_+ F\eta_-}{RT}\right)] \tag{6a}$$

$$FD_{Fe^{3+}}\left(\frac{c^e_{Fe^{3+}}-c^s_{Fe^{3+}}}{r_p}\right) = Fk_+(c^e_{Fe^{2+}})^{(1-\alpha_+)}(c^e_{Fe^{3+}})^{\alpha_+}\left[\left(\frac{c^s_{Fe^{2+}}}{c^e_{Fe^{2+}}}\right)\exp\left(\frac{(1-\alpha_+)F\eta_-}{RT}\right)- \right.$$

$$\left(\frac{c^s_{Fe^{3+}}}{c^e_{Fe^{3+}}}\right)\exp\left(\frac{-\alpha_+ F\eta_-}{RT}\right)] \tag{6b}$$

$$j_- = a_-Fk_-(c_{OH^-})^{(1-\alpha_-)}(c_{Zn(OH_4)^{2-}})^{\alpha_-}\left[\left(\frac{c_{OH^-}}{c_{OH^-,ref}}\right)^4\left(\frac{M_{Zn}}{M_{Zn,ref}}\right)\exp\left(\frac{2(1-\alpha_-)F\eta_-}{RT}\right)- \right.$$

$$\left(\frac{c_{Zn(OH_4)^{2-}}}{c_{Zn(OH_4)^{2-},ref}}\right)\exp\left(\frac{-2\alpha_- F\eta_-}{RT}\right)] \tag{6c}$$

where j is the local reaction current density, a and r_p are the specific surface area and average pore radius of the porous electrode, respectively. k and α are the standard reaction rate constant and charge transfer coefficient, respectively. c^s_i denotes the surface concentration of species i at the electrolyte-electrode interface. The overpotential η is defined by:

$$\eta_j = \phi^e_l - \phi^e_s - E_{0,j} \tag{7}$$

where $E_{0,j}$ denotes the open-circuit voltage and is calculated using the Nernst equations:

$$E_{0,-} = E'_{0,-} + \frac{RT}{nF}\ln\left(\frac{c^e_{Fe^{3+}}}{c^e_{Fe^{2+}}}\right) \tag{8}$$

$$E_{0,+} = E'_{0,+} + \frac{RT}{nF}\ln\left(\frac{c^e_{Zn(OH_4)^{2-}}}{c^e_{OH^-}{}^4}\right) \tag{9}$$

The volume of the negative electrode varies ascribed to the zinc deposition during charging, which is given by:

$$\frac{\partial\varepsilon}{\partial t} = \frac{1}{2F}\frac{MW^{Zn}}{\rho^{Zn}}a_-i_- \tag{10}$$

where MW and ρ denote the molecular weight and density, respectively.

The porosity and specific surface area also change when zinc deposits fill the pores of the electrode, which is described as:

$$\frac{a}{a_0} = 1 - \left(\frac{\varepsilon_p}{\varepsilon}\right)^{0.5} \tag{11}$$

where a_0 and ε_p denote the initial specific surface area and the volume fraction

9

203 of the solid products, respectively.

204

2.1.2 Boundary conditions

206 At the inlet and outlet of both electrodes, the electrolyte fluxes are defined by the

207 following relations, flux driven by diffusion is supposed to be zero at the exits:

$$y = 0 (inlet) \quad -\vec{n} \cdot \vec{v} = \frac{Q}{\varepsilon w_g t_g} \tag{12}$$

$$y = h_g (outlet) \quad -\vec{n} \cdot D_i^{eff} \nabla c_i^e = 0 \tag{13}$$

210 where w_g and t_g are the width and thickness of the electrode, respectively. Q

211 represents the volumetric flow rate.

212 At the bipolar plates, the boundary conditions in the charging process are

213 expressed as:

$$-\vec{n} \cdot \vec{J}_s^{bp} = \begin{cases} -\dfrac{I}{h_g w_g} & x = x_2 \\ \dfrac{I}{h_g w_g} & x = x_5 \end{cases} \tag{14}$$

215 where the applied current I is set as constant, and the sign is reversed during discharge.

216 The grounding condition is applied to the negative bipolar plate:

$$\phi_s^{bp} = 0 \quad x = x_2 \tag{15}$$

218 The boundary condition at the boundaries between the membrane and the porous

219 electrode domains is set up by the following relation:

$$\phi_l^m = \phi_l^e - \frac{RT}{z_i F} \ln(\frac{c_i^m}{c_i^e}) \tag{16}$$

221 where c_i^m is the species concentration in the membrane. The potential shift caused by

222 the above equation is called the Donnan potential [48].

2.2 Shunt current model

224 An electrical circuit analog is adopted to describe the shunt losses caused by the

225 electrolyte bypassing flow through pipes. The cell is represented by an ideal voltage

226 source and a resistor in series. The channels and manifolds are represented by

227 equivalent resistors. During calculations, the electronic potentials of all cells are

228 assumed to be identical, so are the channels and manifolds. The electronic and ionic

229 potential inside each electrode is assumed to be uniform, and shunt losses between

230 modules are not considered.

231   The values of the equivalent resistors can be calculated through the following

232 equation [49]:

$$\text{r} = \frac{1}{\sigma}\frac{l}{s} \tag{17}$$

234 in which l is the length of the flow path, s is the cross-sectional area, and σ is the

235 electrolyte conductivity.

236   The Kirchhoff's loop law is employed to calculate the values and directions of

237 current flow through each resistor. The total power losses are given as below:

$$\text{W}_S = \sum \text{I}^2 r \tag{18}$$

239 **2.3 Pumping loss model**

240   The inlet electrolytes flow through the polyvinyl chloride (PVC) frame and across

241 the porous electrode. The pressure drop of the cell can therefore be defined by Darcy's

242 law [36]:

$$\Delta P_e = \frac{L}{w_g}\frac{\mu Q}{t_g K} \tag{19}$$

244 in which L denotes the length of the flow path through the porous electrode, μ denotes

245 the electrolyte dynamic viscosity. The permeability coefficient of the porous electrode

246 (K) can be calculated using the Kozeny–Carman equation [50]:

$$247 \qquad K = \frac{d^2}{C} \frac{\varepsilon^{m+1}}{(1-\varepsilon)^m} \qquad (20)$$

248   where d represents the diameter of the fiber, C and m are geometry coefficients taken

249   as 0.07025 and 0.2282 obtained from experimental tests [50], respectively.

250   The pressure drop from each channel and manifold can be determined via the

251   Hagen-Poiseuille equation [36]:

$$252 \qquad \Delta P = \frac{128 \mu Q}{\pi d_H^4} \qquad (21)$$

253   where d_H represents the hydraulic diameter of the flow channel.

254   Since the flow rates of the negative and positive sides are identical, the total power

255   losses can be calculated by:

$$256 \qquad W_P = \frac{2 \Delta P Q}{\eta} \qquad (22)$$

257   where η is the pump efficiency and is taken as a constant of 67% [40].

258   It is worth noting that while the side reaction HER happens or the electrode

259   porosity changes with the zinc dissolution-deposition, the pressure of the cell changes

260   simultaneously, the neglect of which may contribute to the discrepancy between the

261   model and experimental data. These factors can be amplified especially when it comes

262   to a stack and should be paid attention to during practical engineering.

263   **2.4 Capital cost model**

264   The system cost is comprised of two parts: electrolyte cost and stack cost, which

265   is given by the following equation [40]:

$$266 \qquad C_{sys} \approx C_e + C_s = \frac{U_e}{V_{eff}} + \frac{U_s}{ti V_{eff}} \qquad (23)$$

267   where C_{sys}, C_e and C_s are the system, electrolyte, and stack costs, respectively. U_e

268   denotes the unit price of the redox species and supporting electrolytes, U_s the unit

269   price of the stack components accounting for electrodes, membranes, and bipolar plates,

270   t the designed discharge duration, and i the current density. V_{eff} represents the

271   effective discharge voltage and is given as [36]:

272
$$V_{eff} = V(\frac{VI - W_P - W_S}{VI}) \tag{24}$$

273   where V is the operating voltage at the SOC of 50%, which is determined from the

274   electrochemical model.

275   The system efficiency is defined as the energy efficiency of the battery system in

276   consideration of shunt loss and pump loss, which is determined by the following

277   equation:

278
$$\eta_S = \frac{VI - W_P - W_S}{VI} \tag{25}$$

279   **2.5 Membrane Model**

280   The mechanisms of the ion exchange membrane and the porous membrane are

281   different. Ion exchange membranes transfer counter ions and isolate active species with

282   permanent fixed space charge, while porous membranes separate active species and

283   charge carrier ions by pore size exclusion [51]. In this model, the fixed space charge

284   concentration of Nafion 212 is 1990 mol m^{-3} and only proton is transferred, while the

285   charge carrier ion of PBI is OH^-. All properties mentioned above are set in the built-

286   in interface of COMSOL.

287   **3. Numerical conditions**

288   **3.1 Calculation details**

289   The parameters utilized for simulation are listed in **Table 1**, **Table 2**, and **Table 3**.

290   The costs for various components are given in **Table 4**.

291   The electrochemical model was simulated via COMSOL Multiphysics software

292   utilizing the tertiary current distribution interface. The mesh including 4616 elements

293   and the relative tolerance of 10^{-3} was adopted. The shunt loss, pumping loss, and cost

294   models were solved using MATLAB software.

295   **Table 1** Parameters used in the simulation

Parameter	Symbol	Value	Unit	Ref.
Geometrical properties				
Thickness of the membrane	t_m	3.5×10^{-5}	m	[42]
Thickness of the electrode	t_g	0.007	m	-
Porosity of the electrode	ε	0.94	-	[42]
Fiber diameter of the electrode	d	19.2	μm	[50]
Specific surface area of the electrode	a	5.0×10^4	m^{-1}	-
Height of the cell	h_g	0.06	m	[42]
Width of the cell	w_g	0.08	m	[42]
Channel height	-	0.006	m	-
Channel width	-	0.01	m	-
Channel length	-	0.2	m	-
Manifold diameter	-	0.04	m	-
Manifold segment length	-	0.007	m	-
Electrolyte properties				
Diffusion coefficient of OH⁻	$D_{\mathrm{OH-}}$	5.27×10^{-9}	$m^2\,s^{-1}$	[52]
Diffusion coefficient of K⁺	$D_{\mathrm{K+}}$	1.96×10^{-9}	$m^2\,s^{-1}$	[52]
Diffusion coefficient of Na⁺	$D_{\mathrm{Na+}}$	1.33×10^{-9}	$m^2\,s^{-1}$	[52]
Diffusion coefficient of $Zn(OH)_4^{2-}$	$D_{\mathrm{Zn(OH)_4^{2-}}}$	3.10×10^{-10}	$m^2\,s^{-1}$	[52]
Diffusion coefficient of $Fe(CN)_6^{4-}$	$D_{\mathrm{Fe(CN)_6^{4-}}}$	7.35×10^{-10}	$m^2\,s^{-1}$	[52]
Diffusion coefficient of $Fe(CN)_6^{3-}$	$D_{\mathrm{Fe(CN)_6^{3-}}}$	8.96×10^{-10}	$m^2\,s^{-1}$	[52]
OH⁻ initial concentration in negative electrolyte	$c_{-,\mathrm{OH-}}^0$	4000	$mol\,m^{-3}$	[42]

OH⁻ initial concentration in positive electrolyte	$c^0_{+,OH-}$	3000	mol m^{-3}	[42]
$Zn(OH)_4^{2-}$ initial concentration in negative electrolyte	$c^0_{Zn(OH)_4^{2-}}$	250	mol m^{-3}	-
Zn initial concentration in negative electrolyte	c^0_{Zn}	250	mol m^{-3}	-
Na⁺ initial concentration in negative electrolyte	$c^0_{-,Na+}$	4000	mol m^{-3}	[42]
Na⁺ initial concentration in positive electrolyte	$c^0_{+,Na+}$	1000	mol m^{-3}	[42]
$Fe(CN)_6^{4-}$ initial concentration in positive electrolyte	$c^0_{Fe(CN)_6^{4-}}$	500	mol m^{-3}	-
$Fe(CN)_6^{3-}$ initial concentration in positive electrolyte	$c^0_{Fe(CN)_6^{3-}}$	500	mol m^{-3}	-
K⁺ initial concentration in positive electrolyte	c^0_{K+}	3000	mol m^{-3}	[42]

296

Table 2 Kinetic parameters used in the simulation

Parameter	Symbol	Value	Unit
Anodic transfer coefficients of negative reaction, charge	$\alpha^a_{-,cha}$	0.6	-
Cathodic transfer coefficients of negative reaction, charge	$\alpha^c_{-,cha}$	0.4	-
Anodic transfer coefficients of positive reaction, charge	$\alpha^a_{+,cha}$	0.6	-
Cathodic transfer coefficients of positive reaction, charge	$\alpha^c_{+,cha}$	0.4	-
Anodic transfer coefficients of negative reaction, discharge	$\alpha^a_{-,dis}$	0.5	-
Cathodic transfer coefficients of negative reaction, discharge	$\alpha^c_{-,dis}$	0.5	-
Anodic transfer coefficients of positive reaction, discharge	$\alpha^a_{+,dis}$	0.2	-
Cathodic transfer coefficients of positive reaction, discharge	$\alpha^c_{+,dis}$	0.8	-
Standard rate constant of negative reaction, charge	$k_{-,cha}$	4×10^{-8}	m s^{-1}
Standard rate constant of positive reaction, charge	$k_{+,cha}$	4×10^{-8}	m s^{-1}
Standard rate constant of negative reaction, discharge	$k_{-,dis}$	1×10^{-7}	m s^{-1}
Standard rate constant of positive reaction, discharge	$k_{+,dis}$	6×10^{-5}	m s^{-1}

297

<div align="center">**Table 3** General parameters</div>

Parameter	Symbol	Value	Unit	Ref.
Density of Zn	ρ_{Zn}	7,140	kg m^{-3}	-
Molecular weight of Zn	MW_{Zn}	65.38	g mol^{-1}	-
Operating temperature	T	298.15	K	-
Conductivity of the electrode	σ	300	S m^{-1}	-
Number of transferred electrons of negative reaction	n_-	2	-	-
Number of transferred electrons of positive reaction	n_+	1	-	-
Standard potential of negative reaction	$E'_{0,-}$	-1.41	V	[42]
Standard potential of positive reaction	$E'_{0,+}$	0.33	V	[42]

298

Table 4 Component cost used in the simulation

Component	Cost	Unit	Ref.
Carbon felt	70	$ m^{-2}	[40]
Bipolar plate	55	$ m^{-2}	[36]
PBI membrane	40	$ m^{-2}	[42]
Valves	150	$ per unit	[40]
Pipes	8	$ m^{-1}	[40]
Bolts	15	$ per unit	[40]
Gaskets	2.5	$ per unit	[40]
Collector plates	150	$ per unit	[40]
End plates	193	$ per unit	[40]
PVC pipe 1	8.6	$ ft^{-1}	[40]
PVC pipe 6	285	$ ft^{-1}	[40]
PVC frame	16.56	$ m^{-2}	[40]
Pump cost estimate, base	8343.1	$ per unit	[36]
Pump cost estimate	18	$ GPM^{-1}	[36]
PCS	210	$ kW^{-1}	[40]
Labor	1	$ kWh^{-1}	[40]
Tank	0.41	$ gal^{-1}	[40]
ZnO cost	1.3	$ kg^{-1}	[40]
$Na_4Fe(CN)_6 \cdot 10H_2O$ cost	1.07	$ kg^{-1}	[42]
NaOH cost	0.4	$ kg^{-1}	[40]
KOH cost	0.84	$ kg^{-1}	[42]

3.2 Single-cell model validation

The electrochemical model is validated by comparing the experimental statistics extracted from Yuan's research (points at the current density of 60, 80, 100, and 160 mA cm^{-2}) at 50% SOC, as displayed in **Fig. 2** [42]. The polarization curve is well fitted and shows the correct trend. The slight discrepancies are possibly the result of lacking precise data like reaction rate constants and ignoring the side reactions like HER. Thus, the proposed model can capture the voltage-current relationship of an alkaline Zn-Fe

306 flow battery.

307
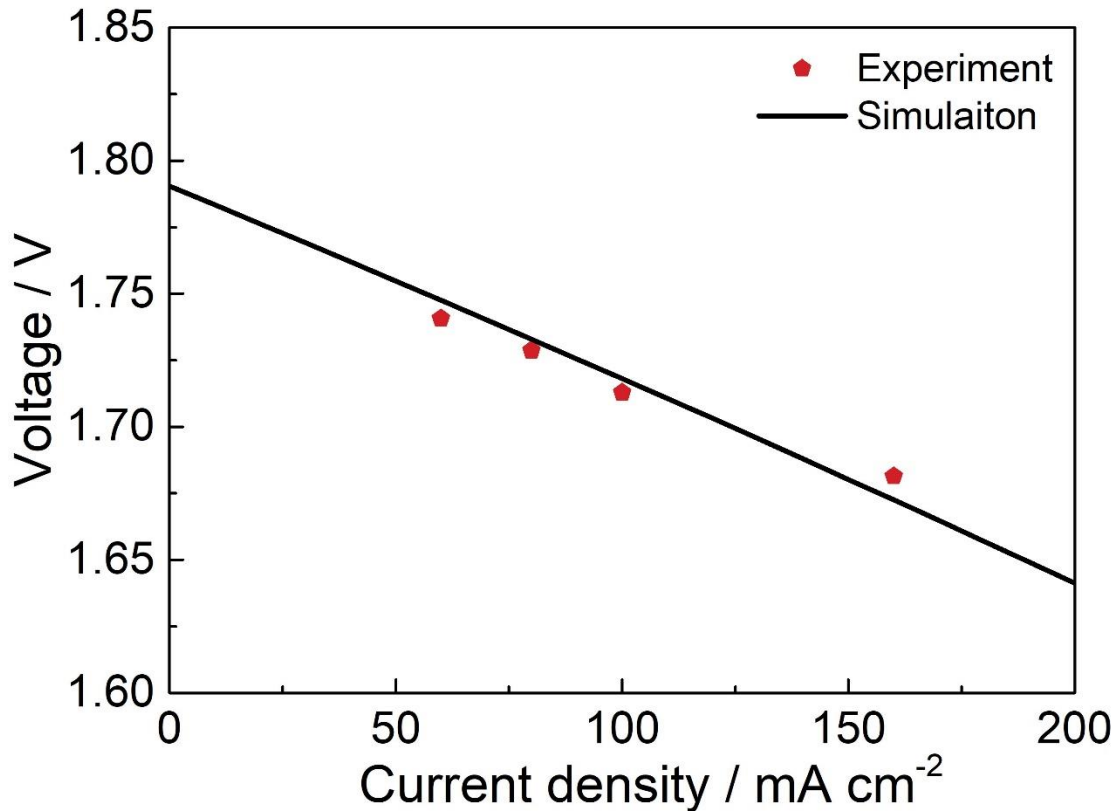
Fig. 2 Comparison of the simulated polarization curve of a zinc-iron flow battery at 50%

SOC with the experimental data.

4. Sensitivity analysis and discussion

4.1 Capital cost

The capital cost of a 0.1 MWh/0.8 MW Zn-Fe flow battery system is shown in **Fig.**

3. At a current density of 35 mA cm^{-2}, a capital cost of 150 $ kWh^{-1} is obtained with the

system energy efficiency of 68%, which satisfies the 2023 DOE's cost target of 150

$ kWh^{-1}. With an increase in the current density, the capital cost is reduced while the

system efficiency decreases at the same time. When the current density goes up to a

larger magnitude, the capital cost under 100 $ kWh^{-1} can be attained, demonstrating its

competitive economy. It is worth noting that the current density is ranging from 20 to

319   200 mA cm^{-2}, since few Zn-Fe flow batteries can work at a quite high current density,

320   at which severe polarization occurs, leading to very low energy efficiency [42].

321   Therefore, tremendous efforts should be made to improve the working current density,

322   such as increasing the specific surface area of electrodes, adopting membranes with

323   high ion conductivity, or improving the conductivity of supporting electrolytes [53].
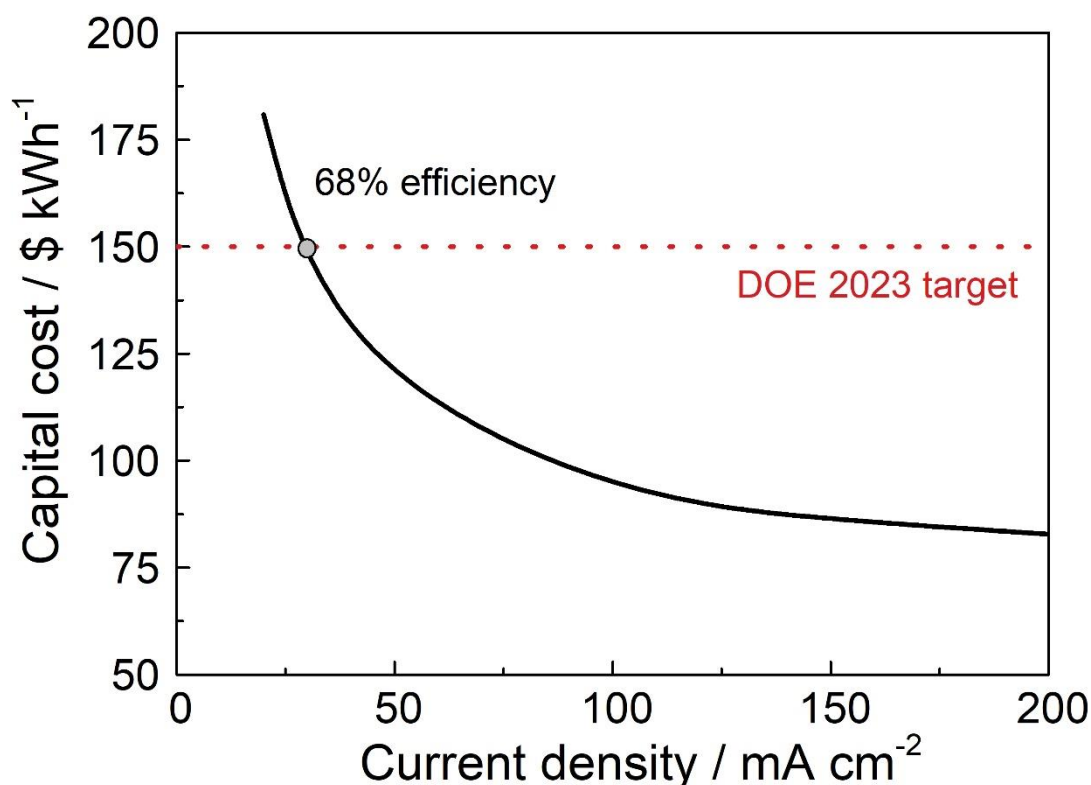
324

325   **Fig. 3** Capital cost for 0.1MW/0.8MWh zinc-iron flow battery system.

326   **4.2 Cost comparisons**

327   To further investigate the capital cost of the Zn-Fe flow battery system, the value

328   is compared with other flow battery systems presented of late, as shown in **Fig. 4** [42].

329   The Zn-Fe system owns the lowest cost with a relatively high power density of 0.247

330   W cm^{-2}, revealing its potential for energy storage applications.

331   **Fig. 5** demonstrates the comparison of the cost breakdown for the V-V, Fe-Cr, and

332   Zn-Fe systems [38]. The Zn-Fe system is the most cost-effective one with a capital cost

333   of 95 \$ kWh^{-1} at the current density of 100 mA cm^{-2}. For both V-V and Zn-Fe systems,

334   the electrolyte is the dominant component and accounts for the cost of 62% and 50%,

335   respectively. While with a high total cost of 229 \$ kWh^{-1}, the electrolyte cost for the V-

336   V system is much higher than that of the Fe-Cr system. Besides, zinc production is as

337   high as 12 million tons per year, while vanadium production is 56000 tons per year [39],

338   making zinc-based batteries more suitable for large-scale production. Compared to the

339   high proportion of membrane cost in the Fe-Cr system (48%), the membrane cost

340   contributes only 9% to the Zn-Fe system, exhibiting the economic advantages of the

341   PBI membrane employed in the Zn-Fe system confronted with the Nafion membrane

342   used for other flow batteries. It should be noted that the system accessories like PVC

343   frame, bipolar plates, gaskets, bolts, and end plates cost totally account for 19% in the

344   Zn-Fe system, which is higher than those in the other two systems, indicating the

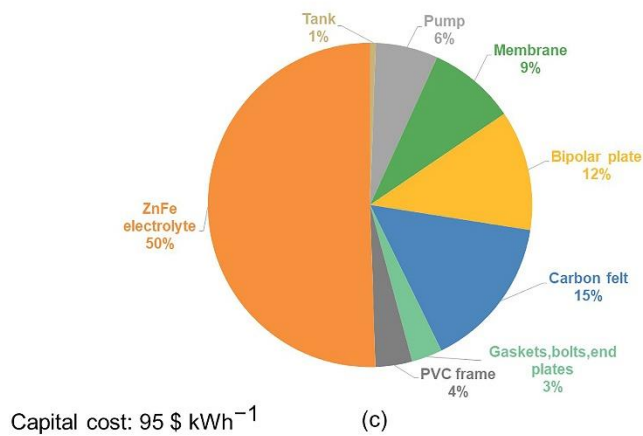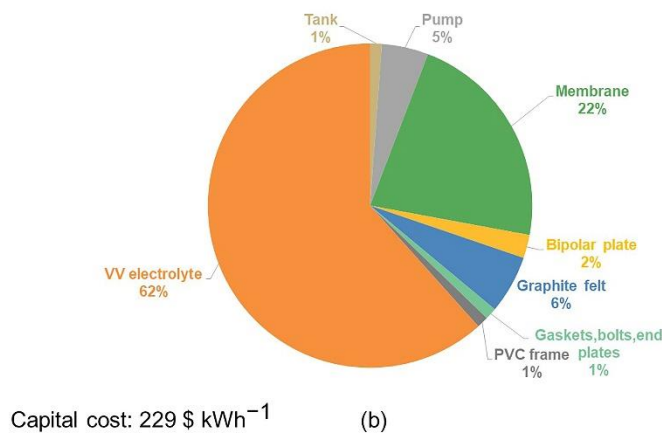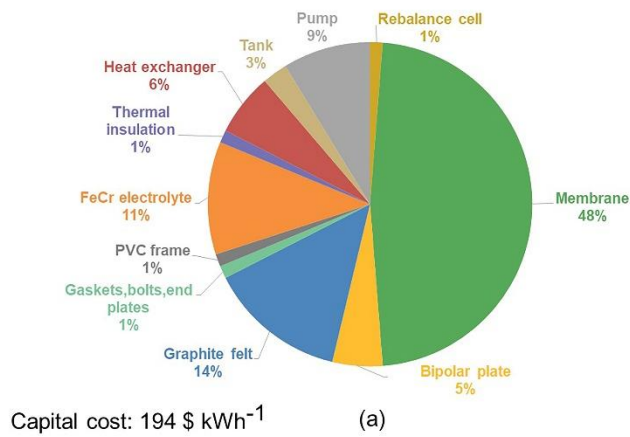345   potential to further reduce the system cost.

346
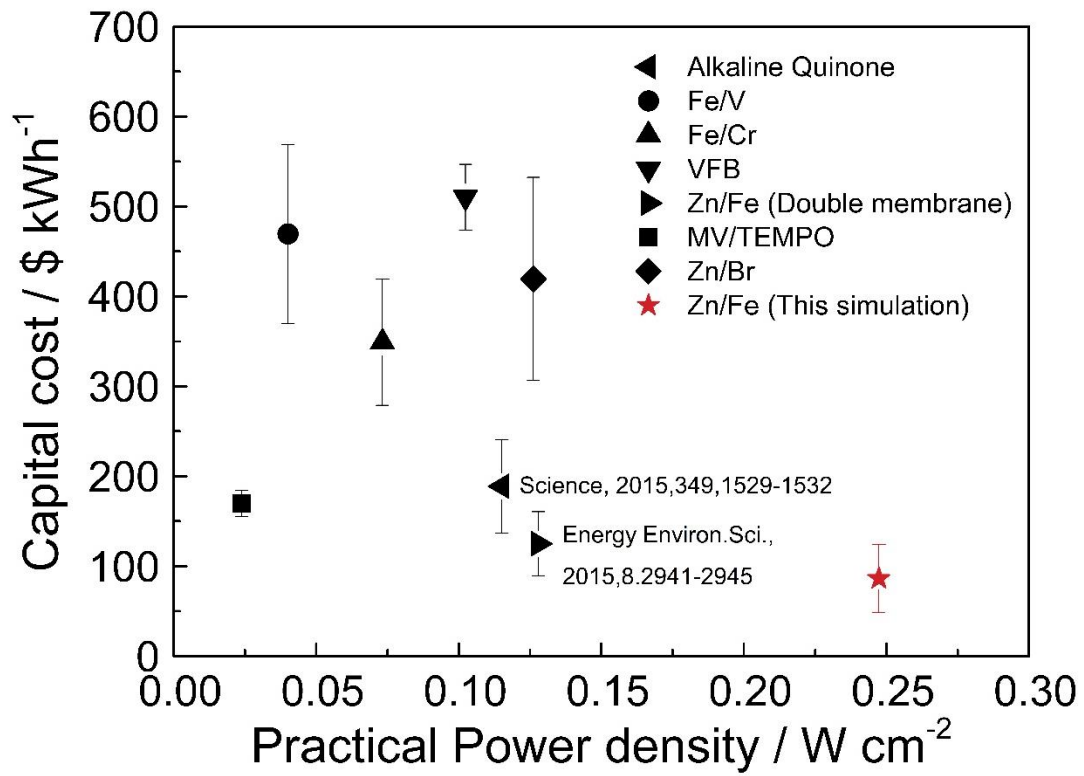
Fig. 4 The cost and practical output power densities for different flow battery systems

(Except as marked on the figure, other data are from [42]).

Capital cost: 194 $ kWh^{-1} (a)

Capital cost: 229 $ kWh^{-1} (b)

Capital cost: 95 $ kWh^{-1} (c)

350

Fig. 5 Capital cost breakdown for different flow battery systems: (a) iron-chromium

system (b) all-vanadium system (c) zinc-iron system.

4.3 Effects of flow rate

The capital cost for the Zn-Fe system is plotted at various flow rates, as displayed

355　in Fig. 6. When the volumetric flow rate rises from 3650 to 6000 ml min^{-1}, the capital

356　cost shows a significant rise from 181 to 297 \$ kWh^{-1} at the current density of 20 mA

357　cm^{-2}. Whereas at a higher current density of more than 100 mA cm^{-2}, the influence of

358　flow rate exhibits quite slight. According to previous research, higher flow rates

359　contribute to faster mass transfer, less concentration polarization, and higher discharge

360　voltages [46]. However, the pump losses also increase to overcome the resistance

361　caused by the increased flow, which reduces the effective voltage and results in a high

362　capital cost. It is worth noting that the working current density of alkaline Zn-Fe flow

363　batteries is ranging from 35 to 160 mA cm^{-2} [53]. In this range, the capital costs of all

364　flow rates are under 150 \$ kWh^{-1}, which meets the DOE's target cost for energy storage

365　technologies. Besides, according to **Fig. 5** (c), the pump cost contributes only 6% to the

366　Zn-Fe system, thereby the increase of system cost causing by higher flow rates to

367　achieve better performance would be small.

368
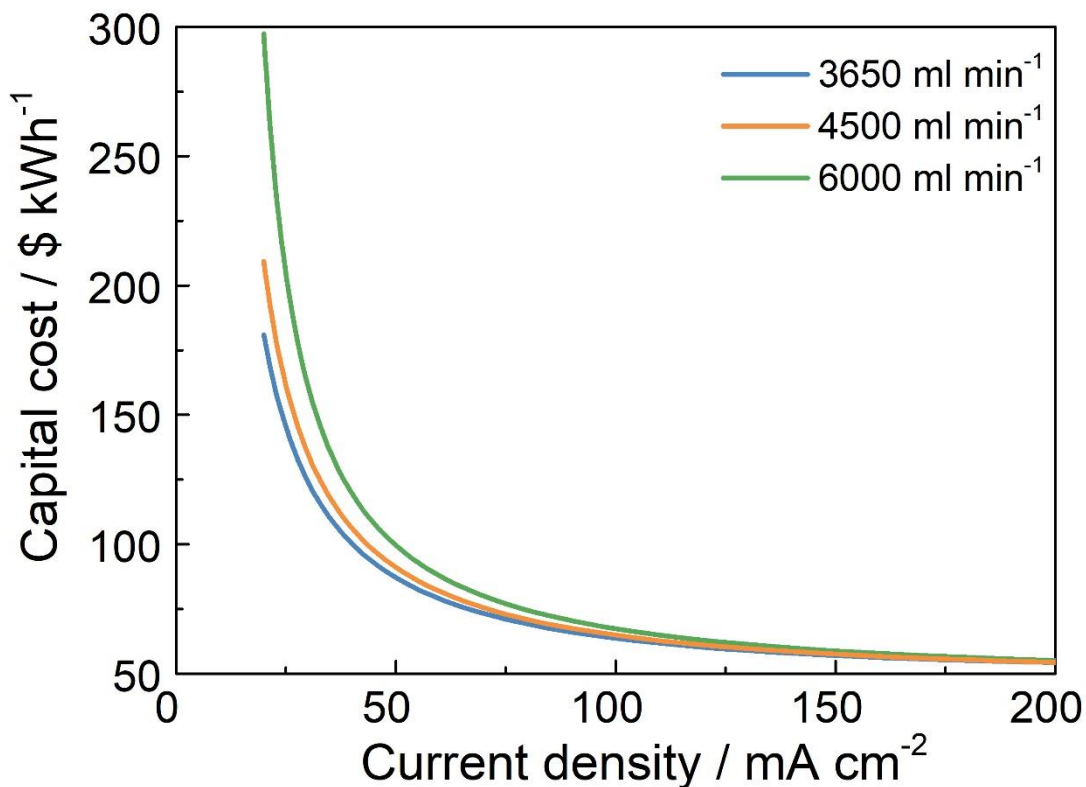
Fig. 6 Capital cost of the system at different flow rates.

4.4 Effects of electrode geometry

4.4.1 Electrode thickness

Fig. 7 (a) displays the influences of electrode thickness on the capital cost. It is evident that the thinner the electrode, the lower the capital cost. This can be explained by that the thicker electrode leads to a longer mass transfer pathway and worse conductivity, which further decreases the discharge voltage. Meanwhile, with a fixed volumetric flow rate, larger electrode thickness results in lower velocity and smaller pump losses, yet this contribution is very slight and offset by the voltage decrease. Especially, at lower current densities of below 25 mA cm^{-2}, the capital costs of the systems with the 3 mm and 7 mm electrodes are approximately identical, indicating limited impacts on the system cost when the electrode thickness is small. It is worth

382 noting that during the calculation, the relationship between the electrode thickness and

383 the unit price of carbon felt is assumed to be linear, which may be more complicated

384 (e.g., the price of a thicker electrode is much higher) in practical. In addition, only the

385 present-day cost of electrodes and other components are considered

386 during calculation, which is based on low volume demand of 50 MW/100

387 MWh [36]. With further industrialization, the electrode price would be lower

388 for rising annual production rates and large-scale purchases, driving

389 the capital cost down.
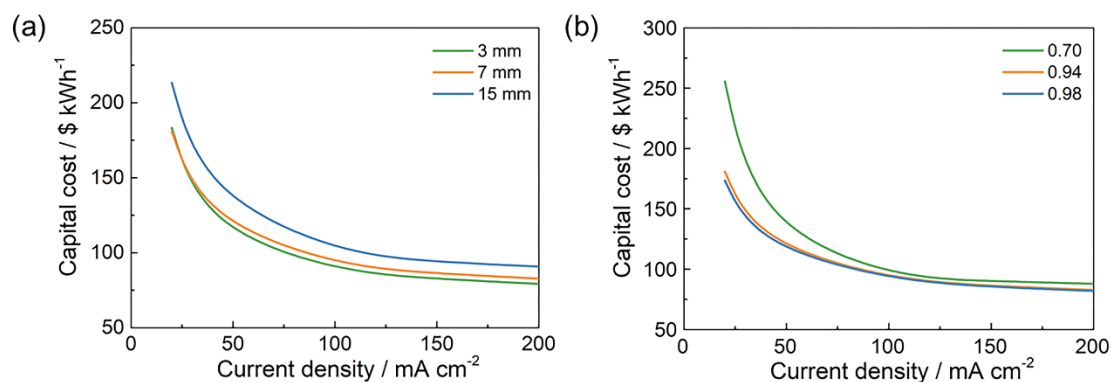
390

391 **Fig. 7** Capital cost of the system with different electrode geometry: (a) electrode

392 thicknesses (b) porosity.

393 **4.4.2 Electrode porosity**

394   **Fig. 7** (b) displays the influences of various porosity on the capital cost with

395 neglecting the variety of carbon felt unit price with the change of porosity. With the

396 electrode porosity increasing from 0.7 to 0.94, a great decline in capital cost is observed

397 among the whole range of the current density. This is because the electrode with higher

398 porosity provides more reaction areas to sufficiently utilize the active species, leading

399 to lower concentration polarization and a higher discharge voltage. In addition, high

26

400 porosity can reduce the pressure drop of the cell, which further decreases the pumping

401 losses. For the system with the electrode porosity of 0.98, the profile is very similar to

402 the system with 0.94 porosity, indicating the slight scope for improvement when the

403 porosity is high enough.

4.5 Effects of membrane

405 The capital costs of the systems with different membranes are displayed in **Fig. 8**.

406 The total cost of the system with the PBI membrane is lower than that with the Nafion

407 212 membrane among the whole range of the current density, which largely benefits

408 from the low unit price of the PBI membrane (40 $ m^{-2}) compared to the Nafion 212

409 membrane (225 $ m^{-2}). Besides, with the current density increasing, the gap between

410 the system costs with two membranes diminishes gradually, which demonstrates that

411 the impact of membranes on the system cost is higher under lower current densities.
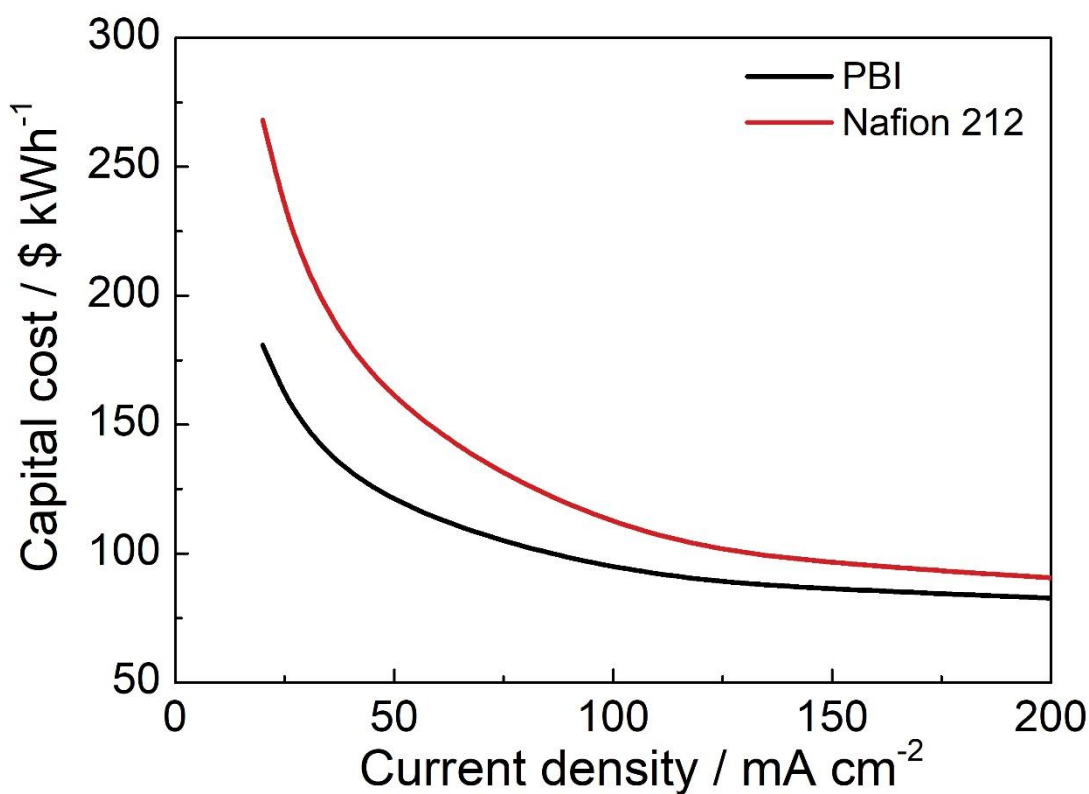
Fig. 8 Capital cost of the system with different membranes.

5. Conclusions

This work reported a cost-performance model for a 0.1 MW/0.8 MWh alkaline zinc-iron flow battery system, including a two-dimensional electrochemical model, a shunt losses model, and a pump losses model. The model validation verifies its ability to predict the correct trend of the voltage-current profiles. A capital cost under 2023 DOE's cost target of 150 $ kWh^{-1} is obtained at the current density of 35 mA cm^{-2}. Compared with other flow battery systems such as all vanadium and iron-chromium flow batteries, the zinc-iron system owns the superiority in cost. Moreover, the influences of the operating conditions, electrode geometry, and cell component on the system cost are investigated. The results indicate that the low current density, low flow rate, high porosity, and thin electrode lead to a low capital cost, while at high current densities, the impacts become smaller. Moreover, the PBI membrane shows better performance on cost than the Nafion 212 membrane. This research can guide the selection of components when constructing a zinc-iron system and design the proper operating conditions, and also be favorable to further reduce the system cost for large-scale energy storage applications.

Declaration of interests

The authors declare no competing interests.

CRediT authorship contribution statement

Ziqi Chen: Conceptualization, Investigation, Methodology, Writing - original draft. **Yongfu Liu**: Investigation. **Wentao Yu**: Investigation, Methodology. **Qijiao He**:

435   Methodology, Writing-review & editing. **Meng Ni**: Supervision, Funding acquisition,

436   Writing - review & editing. **Shuquan Yang**: Investigation, Writing-review & editing.

437   **Shuanglin Zhang**: Investigation, Writing-review & editing. **Peng Tan**: Supervision,

438   Project administration, Funding acquisition, Writing - review & editing.

439   **Acknowledgments**

446   **Nomenclature**

a	specific electroactive area ($m^2\,m^{-3}$)
c	concentration ($mol\,m^{-3}$)
C	special coefficient
d	diameter
D	diffusion coefficient ($m^2\,s^{-1}$)
E_0	equilibrium potential (V)
E_0'	standard reaction potential (V)
F	Faraday constant (96,485 $C\,mol^{-1}$)
h	height
i	current density ($A\,m^{-2}$)
I	current (A)
j	reaction current density ($A\,m^{-2}$)
$\vec{J}$	current density (vector)
k	reaction rate
K	permeability coefficient
L	length (m)
m	special coefficient

29

n	transferred electron
$\vec{n}$	outward normal vector
$\vec{N}$	molar species flux (mol m^{-2} s^{-1})
P	pressure
ΔP	pressure drop
Q	volumetric flow rate (m^3 s^{-1})
r	resistance (Ω)
R	universal gas constant (8.314 J mol^{-1} K^{-1})
s	area (m^2)
S	source (mol m^{-3} s^{-1})
T	temperature (K)
t	component thickness (m)
u	ion mobility
$\vec{v}$	velocity (m s^{-1})
V	voltage (V)
w	component width (m)
W	power
x	distance along cell width (m)
y	distance along cell height (m)
z	valence

447 *Greek*

α	transfer coefficient
η	overpotential (V)/ efficiency
ε	porosity
ρ	density (kg m^{-3})
σ	conductivity (S m^{-1})
μ	dynamic viscosity
ϕ	electric potential (V)

448 *Subscripts*

cell	property of cell
cha	charge
dis	discharge
diff	diffusion
e	electrolyte
eff	effective, corrected for tortuosity
g	electrode
l	liquid or ionic
j	reaction
ref	reference

s	solid or electronic
sys	system
i	specie
$+$	positive half-cell
$-$	negative half-cell

449   *Superscripts*

e	electrode or electrolyte domain
eff	effective value
m	membrane domain
out	outlet
s	surface

450

References

452   [1]   Dovì VG, Friedler F, Huisingh D, Klemeš JJ. Cleaner energy for sustainable
453   future. Journal of Cleaner Production 2009;17:889–95.
454   https://doi.org/10.1016/j.jclepro.2009.02.001.

455   [2]   Yoon SJ, Kim S, Kim DK. Optimization of local porosity in the electrode as an
456   advanced channel for all-vanadium redox flow battery. Energy 2019;172:26–35.
457   https://doi.org/10.1016/j.energy.2019.01.101.

458   [3]   Virulkar V, Aware M, Kolhe M. Integrated battery controller for distributed
459   energy system. Energy 2011;36:2392–8.
460   https://doi.org/10.1016/j.energy.2011.01.019.

461   [4]   Ferreira HL, Garde R, Fulli G, Kling W, Lopes JP. Characterisation of electrical
462   energy storage technologies. Energy 2013;53:288–98.
463   https://doi.org/10.1016/j.energy.2013.02.037.

464   [5]   Zhang Y, Wu Y, You W, Tian M, Huang PW, Zhang Y, et al. Deeply rechargeable
465   and hydrogen-evolution-suppressing zinc anode in alkaline aqueous electrolyte.
466   Nano Letters 2020;20:4700–7. https://doi.org/10.1021/acs.nanolett.0c01776.

467   [6]   Chao D, Zhou W, Xie F, Ye C, Li H, Jaroniec M, et al. Roadmap for advanced
468   aqueous batteries: From design of materials to applications. Science Advances
469   2020;6. https://doi.org/10.1126/sciadv.aba4098.

470   [7]   Sun H, Yu M, Li Q, Zhuang K, Li J, Almheiri S, et al. Characteristics of
471   charge/discharge and alternating current impedance in all-vanadium redox flow
472   batteries. Energy 2019;168:693–701.
473   https://doi.org/10.1016/j.energy.2018.11.130.

474   [8]   Yuan Z, Zhang H, Li X. Ion conducting membranes for aqueous flow battery
475   systems. Chemical Communications 2018;54:7570–88.
476   https://doi.org/10.1039/C8CC03058H.

477   [9]   Chen W, Kang J, Shu Q, Zhang Y. Analysis of storage capacity and energy
478   conversion on the performance of gradient and double-layered porous electrode
479   in all-vanadium redox flow batteries. Energy 2019;180:341–55.
480   https://doi.org/10.1016/j.energy.2019.05.037.

[10] Badrinarayanan R, Tseng KJ, Soong BH, Wei Z. Modelling and control of vanadium redox flow battery for profile based charging applications. Energy 2017;141:1479–88. https://doi.org/10.1016/j.energy.2017.11.082.

[11] Thaller LH. Electrically rechargeable redox flow cells. NASA TM X-71540, Lewis Research Centre, 1974.

[12] Huamin Z, Yu Z, Zonghao L, Xiaoli W. Redox flow battery technology. Progress in Chemistry 2009;21:2333–40. https://doi.org/10.3990/1.9789036532259.

[13] Rychcik M, Skyllas-Kazacos M. Characteristics of a new all-vanadium redox flow battery. Journal of Power Sources 1988;22:59–67. https://doi.org/10.1016/0378-7753(88)80005-3.

[14] Zhou XL, Zeng YK, Zhu XB, Wei L, Zhao TS. A high-performance dual-scale porous electrode for vanadium redox flow batteries. Journal of Power Sources 2016;325:329–36. https://doi.org/10.1016/j.jpowsour.2016.06.048.

[15] Wu Q, Lv Y, Lin L, Zhang X, Liu Y, Zhou X. An improved thin-film electrode for vanadium redox flow batteries enabled by a dual layered structure. Journal of Power Sources 2019;410–411:152–61. https://doi.org/10.1016/j.jpowsour.2018.11.020.

[16] Wei L, Zhao T, Zeng L, Zhou X, Zeng Y. Titanium carbide nanoparticle-decorated electrode enables significant enhancement in performance of all-vanadium redox flow batteries. Energy Technology 2016;4:990–6. https://doi.org/10.1002/ente.201600016.

[17] Oh K, Yoo H, Ko J, Won S, Ju H. Three-dimensional, transient, nonisothermal model of all-vanadium redox flow batteries. Energy 2015;81:3–14. https://doi.org/10.1016/j.energy.2014.05.020.

[18] Sun J, Zheng M, Yang Z, Yu Z. Flow field design pathways from lab-scale toward large-scale flow batteries. Energy 2019;173:637–46. https://doi.org/10.1016/j.energy.2019.02.107.

[19] Yin C, Gao Y, Guo S, Tang H. A coupled three dimensional model of vanadium redox flow battery for flow field designs. Energy 2014;74:886–95. https://doi.org/10.1016/j.energy.2014.07.066.

[20] Vynnycky M. Analysis of a model for the operation of a vanadium redox battery. Energy 2011;36:2242–56. https://doi.org/10.1016/j.energy.2010.03.060.

[21] Leung PK, Ponce-De-León C, Low CTJ, Shah AA, Walsh FC. Characterization of a zinc-cerium flow battery. Journal of Power Sources 2011;196:5174–85. https://doi.org/10.1016/j.jpowsour.2011.01.095.

[22] Cheng J, Zhang L, Yang YS, Wen YH, Cao GP, Wang XD. Preliminary study of single flow zinc-nickel battery. Electrochemistry Communications 2007;9:2639–42. https://doi.org/10.1016/j.elecom.2007.08.016.

[23] Lai Q, Zhang H, Li X, Zhang L, Cheng Y. A novel single flow zinc-bromine battery with improved energy density. Journal of Power Sources 2013;235:1–4. https://doi.org/10.1016/j.jpowsour.2013.01.193.

[24] Yang H, Qiao Y, Chang Z, Deng H, He P, Zhou H. A metal–organic framework as a multifunctional ionic sieve membrane for long-life aqueous zinc–iodide batteries. Advanced Materials 2020;32:1–8.

525 https://doi.org/10.1002/adma.202004240.

[25] Selverston S, Savinell RF, Wainright JS. Zinc-iron flow batteries with common electrolyte. Journal of The Electrochemical Society 2017;164:A1069–75. https://doi.org/10.1149/2.0591706jes.

[26] Zhou X, Lin L, Lv Y, Zhang X, Wu Q. A Sn-Fe flow battery with excellent rate and cycle performance. Journal of Power Sources 2018;404:89–95. https://doi.org/10.1016/j.jpowsour.2018.10.011.

[27] Zeng YK, Zhao TS, Zhou XL, Wei L, Ren YX. A novel iron-lead redox flow battery for large-scale energy storage. Journal of Power Sources 2017;346:97–102. https://doi.org/10.1016/j.jpowsour.2017.02.018.

[28] Zeng YK, Zhao TS, Zhou XL, Wei L, Jiang HR. A low-cost iron-cadmium redox flow battery for large-scale energy storage. Journal of Power Sources 2016;330:55–60. https://doi.org/10.1016/j.jpowsour.2016.08.107.

[29] Zeng YK, Zhao TS, Zhou XL, Zou J, Ren YX. A hydrogen-ferric ion rebalance cell operating at low hydrogen concentrations for capacity restoration of iron-chromium redox flow batteries. Journal of Power Sources 2017;352:77–82. https://doi.org/10.1016/j.jpowsour.2017.03.125.

[30] Gong K, Xu F, Grunewald JB, Ma X, Zhao Y, Gu S, et al. All-soluble all-iron aqueous redox-flow battery. ACS Energy Letters 2016;1:89–93. https://doi.org/10.1021/acsenergylett.6b00049.

[31] Winsberg J, Janoschka T, Morgenstern S, Hagemann T, Muench S, Hauffman G, et al. Poly(TEMPO)/zinc hybrid-flow battery: a novel, "green," high voltage, and safe energy storage system. Advanced Materials 2016;28:2238–43. https://doi.org/10.1002/adma.201505000.

[32] Janoschka T, Martin N, Martin U, Friebe C, Morgenstern S, Hiller H, et al. An aqueous, polymer-based redox-flow battery using non-corrosive, safe, and low-cost materials. Nature 2015;527:78–81. https://doi.org/10.1038/nature15746.

[33] Winsberg J, Hagemann T, Janoschka T, Hager MD, Schubert US. Redox-flow batteries: From metals to organic redox-active materials. Angewandte Chemie - International Edition 2017;56:686–711. https://doi.org/10.1002/anie.201604925.

[34] Yang B, Hoober-Burkhardt L, Wang F, Surya Prakash GK, Narayanan SR. An inexpensive aqueous flow battery for large-scale electrical energy storage based on water-soluble organic redox couples. Journal of The Electrochemical Society 2014;161:A1371–80. https://doi.org/10.1149/2.1001409jes.

[35] Huskinson B, Marshak MP, Suh C, Er S, Gerhardt MR, Galvin CJ, et al. A metal-free organic-inorganic aqueous flow battery. Nature 2014;505:195–8. https://doi.org/10.1038/nature12909.

[36] Viswanathan V, Crawford A, Stephenson D, Kim S, Wang W, Li B, et al. Cost and performance model for redox flow batteries. Journal of Power Sources 2014;247:1040–51. https://doi.org/10.1016/j.jpowsour.2012.12.023.

[37] Grid Energy Storage, U.S. Department of Energy 2013.

[38] Zeng YK, Zhao TS, An L, Zhou XL, Wei L. A comparative study of all-vanadium and iron-chromium redox flow batteries for large-scale energy storage. Journal of Power Sources 2015;300:438–43.

569   https://doi.org/10.1016/j.jpowsour.2015.09.100.

570 [39] Singh N, Mcfarland EW. Levelized cost of energy and sensitivity analysis for the
571   hydrogen bromine flow battery. Journal of Power Sources 2015;288:187–98.
572   https://doi.org/10.1016/j.jpowsour.2015.04.114.

573 [40] Gong K, Ma X, Conforti KM, Kuttler KJ, Grunewald JB, Yeager KL, et al. A
574   zinc-iron redox-flow battery under $100 per kW h of system capital cost. Energy
575   and Environmental Science 2015;8:2941–5. https://doi.org/10.1039/c5ee02315g.

576 [41] Soloveichik GL. Flow batteries: current status and trends. Chemical Reviews
577   2015;115:11533–58. https://doi.org/10.1021/cr500720t.

578 [42] Yuan Z, Duan Y, Liu T, Zhang H, Li X. Toward a low-cost alkaline zinc-iron
579   flow battery with a polybenzimidazole custom membrane for stationary energy
580   storage. iScience 2018;3:40–9. https://doi.org/10.1016/j.isci.2018.04.006.

581 [43] Yuan Z, Liu X, Xu W, Duan Y, Zhang H, Li X. Negatively charged nanoporous
582   membrane for a dendrite-free alkaline zinc-based flow battery with long cycle
583   life. Nature Communications 2018;9:3731. https://doi.org/10.1038/s41467-018-
584   06209-x.

585 [44] Chang N, Yin Y, Yue M, Yuan Z, Zhang H, Lai Q, et al. A cost-effective mixed
586   matrix polyethylene porous membrane for long-cycle high power density
587   alkaline zinc-based flow batteries. Advanced Functional Materials 2019;29:1–
588   11. https://doi.org/10.1002/adfm.201901674.

589 [45] Xie C, Duan Y, Xu W, Zhang H, Li X. A low-cost neutral zinc-iron flow battery
590   with high energy density for stationary energy storage. Angewandte Chemie
591   2017;129:15149–53. https://doi.org/10.1002/ange.201708664.

592 [46] Chen Z, Yu W, Liu Y, Zeng Y, He Q, Tan P, et al. Mathematical modeling and
593   numerical analysis of alkaline zinc-iron flow batteries for energy storage
594   applications.   Chemical   Engineering   Journal   2021;405:126684.
595   https://doi.org/10.1016/j.cej.2020.126684.

596 [47] Dietrich HG, Johnston J. Equilibrium between crystalline zinc hydroxide and
597   aqueous solutions of ammonium hydroxide and of sodium hydroxide. Journal of
598   the   American   Chemical   Society   1927;49:1419–31.
599   https://doi.org/10.1021/ja01405a005.

600 [48] Knehr KW, Kumbur EC. Open circuit voltage of vanadium redox flow batteries:
601   Discrepancy   between   models   and   experiments.   Electrochemistry
602   Communications 2011;13:342–5. https://doi.org/10.1016/j.elecom.2011.01.020.

603 [49] Ratcliff GA. Unit operations of chemical engineering. Chemical Engineering
604   Science 1957;6:287. https://doi.org/10.1016/0009-2509(57)85034-9.

605 [50] Kossenko A, Lugovskoy S, Averbukh M. Electric and hydraulic properties of
606   carbon felt immersed in different dielectric liquids. Materials 2018;11:1–12.
607   https://doi.org/10.3390/MA11040650.

608 [51] Wu J, Dai Q, Zhang H, Li X. Recent development in composite membranes for
609   flow   batteries.   ChemSusChem   2020;13:3805–19.
610   https://doi.org/10.1002/cssc.202000633.

611 [52] J.R. Rumble, Ionic conductivity and diffusion at infinite dilution, CRC

Handbook of Chemistry and Physics, 101st ed. (Internet Version 2020), CRC Press/Taylor &Francis, Boca Raton, FL, 2020.

[53]   Yuan Z, Yin Y, Xie C, Zhang H, Yao Y, Li X. Advanced materials for zinc-based flow battery: development and challenge. Advanced Materials 2019;31:1–27. https://doi.org/10.1002/adma.201902025.